

ThesisTitle

by

Daniel C. Cole

Other Degrees

A thesis submitted to the
Faculty of the Graduate School of the
University of Colorado in partial fulfillment
of the requirements for the degree of
Doctor of Philosophy
Physics Physics
2018

This thesis entitled:
ThesisTitle
written by Daniel C. Cole
has been approved for the Physics Physics

Reader1

Reader2

Date _____

The final copy of this thesis has been examined by the signatories, and we find that both the content and the form meet acceptable presentation standards of scholarly work in the above mentioned discipline.

Cole, Daniel C. (Ph.D., Physics)

ThesisTitle

Thesis directed by Dr. Scott A. Diddams

Optical frequency combs have revolutionized precision metrology by enabling measurements of optical frequencies, with implications both for fundamental scientific questions and for applications such as fast, broadband spectroscopy. In this thesis, I describe the development of comb generation platforms with smaller footprints and higher repetition rates, with the ultimate goal of bringing frequency combs to new applications in a chip-integrated package. I present two new types of frequency combs: electro-optic modulation (EOM) combs and Kerr-microresonator-based frequency combs (microcombs). First I describe the EOM comb scheme and, in particular, techniques for mitigating noise in the comb generation process, and I present the results of a proof-of-principle metrology experiment and some possible applications. Then I discuss developments in microcomb technology. I present novel ‘soliton crystal’ states, which have highly structured ‘fingerprint’ optical spectra that correspond to ordered pulse trains exhibiting crystallographic defects. These pulse trains arise through interaction of the solitons with avoided mode-crossings in the resonator spectrum. Next, I describe the direct and deterministic generation of single microresonator solitons using a phase-modulated pump laser. This technique removes the dependence on initial conditions that was formerly a universal feature of these experiments, presenting a solution to a significant technical barrier to the practical application of microcombs. I also discuss generation of Kerr combs in the Fabry-Perot (FP) geometry. I introduce a nonlinear partial differential equation describing dynamics in an FP cavity and discuss the differences between the FP geometry and the ring cavity, which is the geometry used in previous Kerr-comb experiments. Finally, I discuss a technique for reducing the repetition rate of a high-repetition-rate frequency comb, which will be a necessary post-processing step for some applications. I conclude with a discussion of avenues for future research, including the chip-integration of Fabry-Perot Kerr resonators and the use of band-engineered photonic crystal cavities to further simplify soliton generation.

Acknowledgements

The work in this thesis would not have been possible...

- Acknowledgement line 1
- Acknowledgement line 2

Contents

1	Introduction to microresonator-based frequency combs	1
1.1	Optical microring resonators	1
1.1.1	Resonant enhancement in a microring resonator	3
1.1.2	Thermal effects in microresonators	3
1.2	Microring resonator Kerr frequency combs	4
1.2.1	A model for Kerr-comb nonlinear optics: The Lugiato-Lefever equation	6
1.2.2	Analytical investigation of the resonator's CW response	8
1.2.3	Kerr comb outputs: extended modulation-instability patterns	10
1.2.4	Kerr comb outputs: solitons	12
A	Numerical simulations of nonlinear optics	17
A.1	RK4IP algorithm	17
A.2	Adaptive step-size algorithm	18
A.3	Pseudocode for numerical simulation with the RK4IP algorithm and adaptive step size	18
A.3.1	Simulation of the LLE	19
A.3.2	Simulation of the GNLSE	19
	References	21

Figures

1.1	Optical microdisk resonator	2
1.2	Thermal bistability in microresonators	5
1.3	An illustration of four-wave mixing and frequency-comb generation.	6
1.4	Solution space for the Lugiato-Lefever equation	8
1.5	Investigation of the circulating CW power in a Kerr resonator	9
1.6	Extended-pattern solutions to the LLE	11
1.7	Soliton solutions to the LLE	13
1.8	Kerr-soliton energy-level diagram	14

Chapter 1

Introduction to microresonator-based frequency combs

This chapter introduces the basic physics of optical frequency-comb generation in Kerr-nonlinear microresonators, with a particular emphasis on providing context for the results described in the subsequent chapters. The field is rich and evolving rapidly, and there are facets that are not discussed here; we note that a number of papers that review this topic have been published, each of which provides a unique perspective [1–4].

For simplicity, and following the terminology of the field, we will refer to broadband optical spectra generated through frequency conversion in Kerr-nonlinear resonators as ‘Kerr combs,’ even when the output is not strictly a coherent frequency comb. So far researchers have focused on Kerr-comb generation using microresonators with a ring geometry—so-called microring resonators. It is also possible to generate Kerr combs in a Kerr-nonlinear Fabry-Perot (FP) cavity, as has been recently demonstrated by Obrzud, Lecomte, and Herr [5]. Theoretical investigations of Kerr-comb generation with the FP geometry are presented in Chapter ??.

1.1 Optical microring resonators

An optical microring resonator guides light around a closed path in a dielectric medium by total internal reflection. The principle is the same as the guiding of light in an optical fiber, and indeed a ‘macroring’ resonator can be constructed from a loop of fiber, using a fiber-optic coupler with a small coupling ratio as an input/output port. Microring resonators can be constructed by looping an optical waveguide back on itself, in which case the resonator provides index contrast and light confinement over a full 360° of the modal cross-section. Alternatively, resonators can be realized with geometries that lack an inner radius dimension and therefore provide less spatial confinement. In this case they can host ‘whispering-gallery modes,’ so-called due to their similarity with the acoustic ‘whispering-gallery’ waves that permit a listener on one side of St. Paul’s cathedral (for example) to hear whispers uttered by a speaker on the other side of the cathedral. A schematic depiction of the basic components of a typical microring-resonator experiment is shown in Fig. 1.1. Optical microring resonators have a host of characteristics that make them useful for nonlinear optics and photonics applications; these include the ease with which they can be integrated, the ultra-high quality (Q) factors that have been demonstrated, and the ability to tailor the spectral distribution of guided modes through careful resonator design.

A microring resonator supports propagating guided modes of electromagnetic radiation with (vacuum) wavelengths that evenly divide the optical round-trip path length: $\lambda_m = n_{eff}(\lambda_m)L/m$, with associated resonance frequencies $\nu_m = c/\lambda_m = mc/n_{eff}(\nu_m)L$. This leads to constructive interference from round trip to round trip. Here m is the azimuthal mode number and the quantity $Ln_{eff}(\lambda_m)$ is the optical round-trip path length of the mode, where $n_{eff}(\lambda_m)$ defines an effective index of refraction related to the mode’s propagation constant $\beta_{prop}(\omega)$ via $\beta_{prop}(\omega) = n_{eff}(\omega)\omega/c$ (see e.g. Refs. [8, 9]; we use the subscript *prop* to remove ambiguities arising from the standard use of the symbol β for multiple quantities). The free-spectral range f_{FSR} of a resonator is the *local*

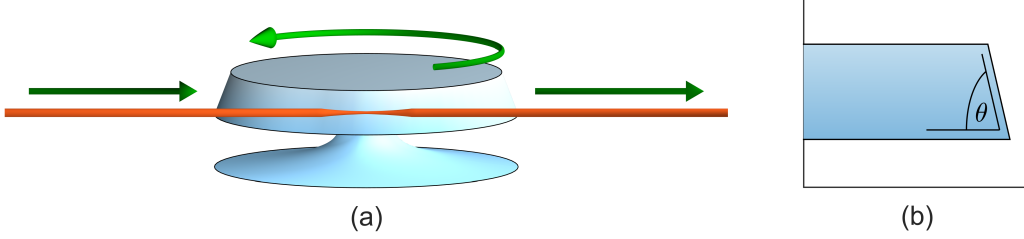


Figure 1.1: **Optical microdisk resonator.** (a) An optical microring resonator with the disk geometry as described in Ref. [6], operated in a through-coupled configuration. Light is evanescently coupled into and out of the resonator through a tapered optical fiber, shown in orange, which contacts the resonator near the fiber's point of smallest diameter. Light circulates in whispering-gallery modes concentric to the resonator's circumference. (b) The wedge angle θ can be adjusted to control the geometric dispersion of the propagating whispering-gallery modes as described in Ref. [7], as θ dictates, for example, the extent to which larger (longer-wavelength) modes are confined further from the circumference of the wedge.

frequency spacing between modes, calculated via:

$$f_{FSR} \approx \nu_{m+1} - \nu_m \approx \nu_m - \nu_{m-1}, \quad (1.1)$$

$$= \frac{\partial \nu_m}{\partial m}, \quad (1.2)$$

$$= \frac{c}{n_{eff}(\nu)L} - \frac{mc}{n_{eff}^2(\nu)L} \frac{\partial n_{eff}}{\partial \nu} \frac{\partial \nu}{\partial m}, \quad (1.3)$$

so that, rearranging, we obtain:

$$f_{FSR} = \frac{c/L}{\left(n_{eff} + \nu \frac{\partial n_{eff}}{\partial \nu}\right)} = \frac{c}{n_g L} = 1/T_{RT}, \quad (1.4)$$

where $n_g = n_{eff} + \nu \frac{\partial n_{eff}}{\partial \nu}$ is the group velocity of the mode and T_{RT} is the mode's round-trip time. The effective index n_{eff} is frequency dependent due to both intrinsic material dispersion and geometric dispersion, where the latter results for example from different sampling of material properties for different wavelength-dependent mode areas. A frequency-dependent n_{eff} leads to a frequency dependence of n_g and f_{FSR} , and a resulting non-uniform spacing in the cavity modes in frequency despite the linearity of ν_m in m .

Depending on the design, microring resonators can support many transverse mode profiles, or just one. The former is typical of whispering-gallery-mode resonators that lack an inner radius, such as the wedge resonator shown in Fig. 1.1 or free-standing silica microrod resonators [10]; the latter can be readily achieved using chip-integrated single-mode photonic waveguides. For a given resonator geometry, to calculate the frequency-dependent effective index $n_{eff}(\nu)$, thereby enabling calculation of the resonance frequencies and wavelengths, one must solve Maxwell's equations for the resonator geometry. Except in special cases of high symmetry (e.g. a sphere [11]), this is typically done numerically using finite-element modeling tools like COMSOL. The modes of an optical resonator, both within a mode family defined by a transverse mode profile (such that they differ only by azimuthal mode number) and between mode families, must be orthogonal [12], with no linear coupling between them.

1.1.1 Resonant enhancement in a microring resonator

The lifetime τ_γ of circulating photons in a resonator is fundamental to its fitness for applications. Generally, two processes lead to the loss of circulating photons: intrinsic dissipation that occurs at a rate $1/\tau_{int}$ and out-coupling to an external waveguide that occurs at a rate $1/\tau_{ext}$, leading to a total loss rate of $\tau_\gamma^{-1} = \tau_{ext}^{-1} + \tau_{int}^{-1}$. To understand the quantitative role of these parameters, we consider a cavity mode of frequency ω_0 and amplitude a (normalized such that $|a|^2 = N$, the number of circulating photons) driven by a pump field with frequency ω_p and rotating amplitude $s \propto \exp(i\omega_p t)$ (normalized such that $|s|^2 = S$, the rate at which photons in the coupling waveguide pass the coupling port) that is in-coupled with strength κ . The equation of motion for such a system is [12]:

$$\frac{da}{dt} = i\omega_0 a - \left(\frac{1}{2\tau_{int}} + \frac{1}{2\tau_{ext}} \right) a + \kappa s. \quad (1.5)$$

We can immediately solve this equation by assuming that $a \propto \exp(i\omega_p t)$, and we obtain:

$$a = \frac{\kappa s}{\left(\frac{1}{2\tau_{int}} + \frac{1}{2\tau_{ext}} \right) + i(\omega_p - \omega_0)}. \quad (1.6)$$

The time-reversal symmetry that is inherent in this system when there is no dissipation, i.e. when $1/\tau_{int} = 0$, can be exploited to show that $|\kappa|^2 = 1/\tau_{ext}$ [12]. By squaring Eq. 1.6 and inserting this expression, we find:

$$N = \frac{\Delta\omega_{ext} S}{\Delta\omega_{tot}^2/4 + (\omega_p - \omega_0)^2}, \quad (1.7)$$

where we have defined the rates $\Delta\omega_{ext} = 1/\tau_{ext}$, $\Delta\omega_{int} = 1/\tau_{int}$, and $\Delta\omega_{tot} = \Delta\omega_{ext} + \Delta\omega_{int}$. Two important observations can be drawn from Eq. 1.7: First, the cavity response is Lorentzian with a full-width at half-maximum (FWHM) linewidth that is related to the photon lifetime via $\tau_\gamma = 1/\Delta\omega_{tot}$, and second, on resonance the number of circulating photons is related to the input rate by the factor $\Delta\omega_{ext}/\Delta\omega_{tot}^2$. The consequences of this second point can be elucidated by calculating the circulating power $P = N\hbar\omega_p/T_{RT}$ on resonance (when $\omega_p = \omega_0$):

$$P = \frac{4\Delta\omega_{ext} P_{in}/T_{RT}}{\Delta\omega_{tot}^2} \quad (1.8)$$

$$= \frac{2P_{in}}{\pi} \eta \mathcal{F}, \quad (1.9)$$

where $\mathcal{F} = 2\pi\tau_\gamma/T_{RT} = f_{FSR}/\Delta\nu$ is the resonator finesse, $\eta = \Delta\omega_{ext}/\Delta\omega_{tot}$ is the coupling ratio, and $P_{in} = \hbar\omega_p S$ is the power in the waveguide. Thus, the circulating power is approximately a factor \mathcal{F} greater than the input power. The combination of this resonant enhancement and a small cavity mode volume enables very large circulating optical intensities in high finesse resonators, which is important for the application of microresonators in nonlinear optics. A second useful figure of merit that is related to the threshold for nonlinear optics is the quality factor $Q = \omega_0\tau_\gamma = \nu_0/\Delta\nu$.

1.1.2 Thermal effects in microresonators

In a typical microresonator frequency-comb experiment, a frequency-tunable pump laser is coupled evanescently into and out of the resonator using a tapered optical fiber [13] (for e.g. free-standing silica disc resonators) or a bus waveguide (for chip-integrated resonators, e.g. in silicon nitride rings). When spatial overlap between the evanescent mode of the coupler and a whispering-gallery mode of the resonator is achieved, with the frequency of the pump laser close to the resonant frequency of that mode, light will build up in the resonator and the transmission of the pump laser past the resonator will decrease.

In any experiment in which a significant amount of pump light is coupled into a resonator, one immediately observes that the cavity resonance lineshape in a scan of the pump-laser frequency is not Lorentzian as expected from Eq. 1.7; plots of measured resonance lineshapes are shown in

Fig. 1.2a. This is due to heating of the resonator as it absorbs circulating optical power. Since the volume of a pumped mode and the physical volume of the microresonator are both small, thermal effects have significant practical implications in microresonator experiments. As the volume of the mode heats (over a ‘fast thermal timescale’) and this energy is conducted to and heats the rest of the resonator (over the ‘slow thermal timescale’) [14], the resonance frequency of a given cavity mode shifts due to the thermo-optic coefficient $\partial n/\partial T$ and the coefficient of thermal expansion of the mode volume $\partial V/\partial T$. For typical microresonator materials the thermo-optic effect dominates, and $\partial n/\partial T > 0$ leads to a decrease in the resonance frequency with increased circulating power in steady state.

A calculation of the thermal dynamics of the system composed of the pump laser and the resonator reveals that near the ‘cold-cavity’ resonance frequency of a given cavity mode the system has three possible thermally-shifted resonance frequencies $\omega_{0,shifted}$ at which thermal steady state is achieved [15]. Generally, these points are:

- (1) $\omega_p > \omega_{0,shifted}$, blue detuning with significant coupled power and thermal shift
- (2) $\omega_p < \omega_{0,shifted}$, red detuning with significant coupled power and thermal shift
- (3) $\omega_p \ll \omega_0$, red detuning with insignificant coupled power and insignificant thermal shift

These points are depicted schematically in Fig. 1.2b. Steady-state point (1) is experimentally important, because in the presence of pump-laser frequency and power fluctuations it leads to so-called thermal ‘self-locking.’ Specifically for steady-state point (1), this can be seen as follows:

- If the pump-laser power increases the cavity heats, the resonance frequency decreases, the detuning increases, and the change in coupled power is minimized.
- If the pump-laser power decreases the cavity cools, the resonance frequency increases, the detuning decreases, and the change in coupled power is minimized.
- If the pump-laser frequency increases the cavity cools, the resonance frequency increases, and the change in coupled power is minimized.
- If the pump-laser frequency decreases the cavity heats, the resonance frequency decreases, and the change in coupled power is minimized.

This is in contrast with steady-state point (2), where each of the four pump-laser fluctuations considered above generates a positive feedback loop, with the result that any fluctuation will push the system towards point (1) or point (3). This preference of the system to occupy point (1) or point (3) over a range of pump-laser detuning is referred to as thermal bistability. One consequence of this bistability is that the transmission profile of the pump laser takes on hysteretic behavior in a scan over a cavity resonance with significant pump power: in a decreasing frequency scan, the lineshape takes on a broad sawtooth shape, while in an increasing frequency scan, the resonance takes on a narrow pseudo-Lorentzian profile whose exact shape depends on the scan parameters relative to the thermal timescale. A second consequence is that, in the absence of other stabilizing effects, operation at red detuning with significant coupled power in a microresonator experiment requires special efforts to mitigate the effects of thermal instability.

1.2 Microring resonator Kerr frequency combs

The high circulating optical intensities accessible in resonators with long photon lifetimes find immediate application in the use of microresonators for nonlinear optics. The experiments described in this thesis are conducted in silica microresonators. Silica falls into a broader class of materials that exhibit both centro-symmetry, which dictates that the second-order nonlinear susceptibility $\chi^{(2)}$ must vanish, and a significant third-order susceptibility $\chi^{(3)}$. The n^{th} -order susceptibility is a term in the Taylor expansion describing the response of the medium’s polarization to an external

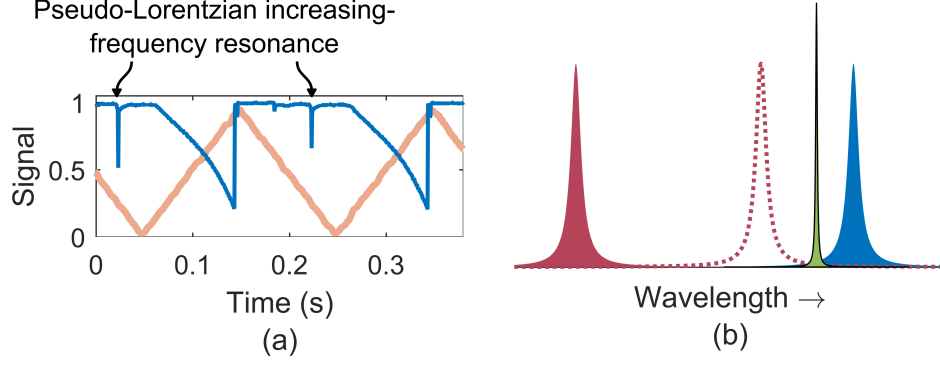


Figure 1.2: **Thermal bistability in microresonators.** (a) Measurement of power transmitted past the microresonator (blue) in an experiment using a ~ 16.5 GHz-FSR microdisk resonator and a tapered fiber. The wavelength of the pump laser is controlled by a piezo-electric crystal that adjusts the length of the laser cavity. Here, larger control signal (orange) corresponds to longer laser wavelength. As the laser wavelength is increased, the resonator heats and a sawtooth-shaped resonance is observed. Ultimately the resonator reaches a maximum temperature that depends on the pump power, and the laser then becomes red-detuned as the wavelength continues to increase; then the resonator rapidly cools and the resonance is lost. Shortly thereafter, the direction of the scan is reversed. As the resonator wavelength is decreased, the system will ‘flip’ from steady-state point (3) to steady-state point (1), leading to observation of a narrow pseudo-Lorentzian resonance, with the exact shape depending on the thermal and scanning timescales. (b) Depiction of the three steady-state points for the laser detuning. For fixed laser wavelength (green), stable steady-state points exist with relatively small blue detuning and significant coupled power (solid blue), and relatively large red detuning and little coupled power (solid red). An unstable steady-state point also exists with red detuning and significant coupled power (dashed red). Note in this terminology that the color of the detuning (red or blue) refers to the position of the laser relative to the position of the resonance in wavelength space.

electric field [16]: $P = P_0 + \epsilon_0 \chi^{(1)} E + \epsilon_0 \chi^{(2)} E^2 + \epsilon_0 \chi^{(3)} E^3 + \dots$. The effect of $\chi^{(3)}$ can be described in a straightforward way as a dependence of the refractive index on the local intensity [8],

$$n = n_0 + n_2 I \quad (1.10)$$

where $n_2 = \frac{3\chi^{(3)}}{4n_0^2\epsilon_0 c}$ [8, 17]. The intensity-dependence of the refractive index resulting from the third-order susceptibility $\chi^{(3)}$ is referred to as the optical Kerr effect.

The combination of the Kerr effect and the high circulating intensities that are accessible in high- Q cavities provides a powerful platform for nonlinear optics. Specifically, the Kerr effect enables self-phase modulation, cross-phase modulation, and four-wave mixing (FWM), the last of which is depicted schematically in Fig. 1.3.

In 2007, a remarkable result brought about a new era for frequency comb research. Del’Haye et al. reported *cascaded four-wave mixing* (CFWM, shown in Fig. 1.3c) in anomalously-dispersive ($\beta_{prop,2} < 0$) toroidal silica microcavities on silicon chips, the result of which was a set of many co-circulating optical fields that were uniformly spaced by f_{rep} ranging from 375 GHz to ~ 750 GHz (depending on the platform) [18]. Measurements indicated that the frequency spacing was uniform to a precision of 7.3×10^{-18} , thereby establishing that the output of the system was a frequency comb. This result built on previous demonstrations of few-mode parametric oscillation in microresonators [19–21], and showed that the non-uniform distribution of cavity resonance frequencies due to dispersion could be overcome to generate an output with equidistant frequency modes. A second important development occurred in 2012, when Herr et al. reported the generation of frequency

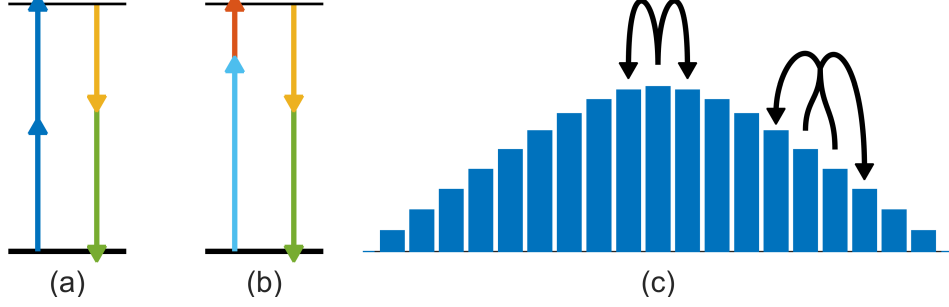


Figure 1.3: **An illustration of four-wave mixing and frequency-comb generation.** (a) Degenerate four-wave mixing, in which two fields of the same frequency ω_1 (blue) mix and generate fields at two new frequencies ω' and ω'' (yellow and green). The schematic indicates the energy-conservation requirements of the process, which can be written as $2\omega_1 = \omega' + \omega''$. (b) Non-degenerate four-wave mixing, in which two fields of different frequencies ω_2 and ω_3 (light blue and orange) mix to generate fields at frequencies ω' and ω'' (yellow and green). Energy conservation is now expressed as $\omega_2 + \omega_3 = \omega' + \omega''$. (c) Schematic depiction of one degenerate FWM step and one non-degenerate FWM step in a cascaded four-wave mixing process that generates a frequency comb. Figure after Ref. [1].

combs corresponding in the time domain to single circulating optical ‘soliton’ pulses [22, 23]. This observation followed the observation of solitons in formally-equivalent passive fiber-ring resonators in 2010 [24]. Due to unique properties that make them particularly well-suited for applications, as discussed in Sec. 1.2.4, the generation and manipulation of soliton combs has become a significant priority in microcomb research.

1.2.1 A model for Kerr-comb nonlinear optics: The Lugiato-Lefever equation

Kerr-comb generation can be motivated and partially understood through the CFWM picture [25], but the phase and amplitude degrees of freedom for each comb line mean that CFWM gives rise to a rich space of comb phenomena—it is now known that Kerr combs can exhibit several fundamentally distinct outputs. A useful model for understanding this rich space is the Lugiato-Lefever equation (LLE), which was shown to describe microcomb dynamics by Chembo and Menyuk [26] through Fourier-transformation of a set of coupled-mode equations describing CFWM and by Coen, Randle, Sylvestre, and Erkintalo [27] through time-averaging of a more formally-appropriate model for a low-loss resonator (as first performed by Haelterman, Trillo, and Wabnitz [28]). The LLE is a nonlinear partial-differential equation that describes evolution of the normalized cavity field envelope ψ over a slow time $\tau = t/2\tau_\gamma$ in a frame parametrized by the ring’s azimuthal angle θ (running from $-\pi$ to π) co-moving at the group velocity. The equation formulated by Chembo and Menyuk, as it will be used throughout this thesis, reads:

$$\frac{\partial \psi}{\partial \tau} = -(1 + i\alpha)\psi + i|\psi|^2\psi - i\frac{\beta_2}{2}\frac{\partial^2 \psi}{\partial \theta^2} + F. \quad (1.11)$$

This equation describes ψ over the domain $-\pi \leq \theta \leq +\pi$ with periodic boundary conditions $\psi(-\pi, \tau) = \psi(\pi, \tau)$. Here F is the strength of the pump laser, with F and ψ both normalized so that they take the value 1 at the absolute threshold for parametric oscillation: $F = \sqrt{\frac{8g_0\Delta\omega_{ext}}{\Delta\omega_{tot}^3} \frac{P_{in}}{\hbar\omega_p}}$, $|\psi|^2 = \frac{2g_0T_{RT}}{\hbar\omega_p\Delta\omega_{tot}} P_{circ}(\theta, \tau)$, so that $|\psi(\theta, \tau)|^2$ is the instantaneous normalized power at the co-moving azimuthal angle θ . Here $g_0 = n_2c\hbar\omega_p^2/n_g^2V_0$ is a parameter describing the four-wave mixing gain, $\Delta\omega_{ext}$ is the rate of coupling at the input/output port, $\Delta\omega_{tot} = 1/\tau_\gamma$ is the FWHM resonance linewidth, P_{in} is the pump-laser power, $P_{circ}(\theta, \tau)$ is the local circulating power in the cavity, \hbar is Planck’s constant, and ω_p is the pump-laser frequency. The parameters n_2 , n_g , and V_0 describe the

nonlinear (Kerr) index (see Eqn. 1.10), the group index of the mode, and the effective nonlinear mode volume at the pump frequency; L is the physical round-trip length of the ring cavity.

The parameters α and β_2 describe the normalized frequency detuning of the pump laser and second-order dispersion of the resonator mode family into which the pump laser is coupled: $\alpha = -\frac{2(\omega_p - \omega_0)}{\Delta\omega_{tot}}$, $\beta_2 = -\frac{2D_2}{\Delta\omega_{tot}}$; here $D_2 = \left. \frac{\partial^2 \omega_\mu}{\partial \mu^2} \right|_{\mu=0}$ is the second-order modal dispersion parameter, where μ is the pump-referenced mode number of Eq. ???. The parameters $D_1 = \left. \frac{\partial \omega_\mu}{\partial \mu} \right|_{\mu=0} = 2\pi f_{FSR}$ and D_2 are related to the derivatives of the propagation constant $\beta_{prop} = n_{eff}(\omega)\omega/c$ via $D_1 = 2\pi/L\beta_1$ and $D_2 = -D_1^2 \frac{\beta_{prop,2}}{\beta_{prop,1}}$, where $\beta_{prop,n} = \partial^n \beta_{prop} / \partial \omega^n$. The subscript *prop* is used here to distinguish the propagation constant from the LLE dispersion coefficients $\beta_n = -2D_n/\Delta\omega_{tot}$, as unfortunately the use of the symbol β for both of these quantities is standard. Expressions for higher-order modal dispersion parameters D_n in terms of the expansion of the propagation constant can be obtained by evaluating the equation $D_{n>1} = (D_1 \frac{\partial}{\partial \omega})^{n-1} D_1$, and may be incorporated into the LLE up to desired order N through the replacement:

$$-i \frac{\beta_2}{2} \frac{\partial^2 \psi}{\partial \theta^2} \rightarrow + \sum_{n=1}^N i^{n+1} \frac{\beta_n}{n!} \frac{\partial^n \psi}{\partial \theta^n}. \quad (1.12)$$

This thesis describes frequency-comb generation in anomalously-dispersive resonators, and so $\beta_2 < 0$ throughout.

The formulation of the LLE in terms of dimensionless normalized parameters helps to elucidate the fundamental properties of the system and facilitates comparison of results obtained in platforms with widely different experimental conditions. The LLE relates the time-evolution of the intracavity field (normalized to its threshold value for cascaded four-wave mixing) to the power of the pump laser (normalized to its value at the threshold for cascaded four-wave mixing), the pump-laser detuning (normalized to half the cavity linewidth), and the cavity second-order dispersion quantified by the change in the FSR per mode (normalized to half the cavity linewidth). One example of the utility of this formulation is that it makes apparent the significance of the cavity linewidth in determining the output comb, and underscores the fact that optimization of the dispersion, for example, without paying heed to the effect of this optimization on the cavity linewidth, may not yield the desired results.

The LLE is, of course, a simplified description of the dynamics occurring in the microresonator. It abstracts the nonlinear dynamics and generally successfully describes the various outputs that can be generated in a microresonator frequency comb experiment. The LLE is a good description of these nonlinear dynamics when the resonator photon lifetime, mode overlap, and nonlinear index n_2 are roughly constant over the bandwidth of the generated comb, and when the dominant contribution to nonlinear dynamics is simply the self-phase modulation term $i|\psi|^2\psi$ arising from the Kerr nonlinearity. The LLE neglects polarization effects, thermal effects, and the Raman scattering and self-steepening nonlinearities, although in principle each of these can be included [8, 23, 29, 30]. It is also worth emphasizing that the LLE can be derived from a more formally-accurate Ikeda map (as is done by Coen et al. [27]), in which the effect of localized input- and output-coupling is included in the model. This is achieved by ‘delocalizing’ the pump field and the output-coupling over the round trip, including only their averaged effects. This is an approximation that is valid in the limit of high finesse due to the fact that the cavity field cannot change on the timescale of a single round trip, but as a result the LLE necessarily neglects all dynamics that might have some periodicity at the round-trip time; the fundamental timescale of LLE dynamics is the photon lifetime.

The LLE provides a useful framework for the prediction and interpretation of experimental results. Basically, it predicts the existence of two fundamentally distinct types of Kerr-combs: extended temporal patterns and localized soliton pulses. These predictions are born out by experiments, the interpretation of which is facilitated by insight gained from the LLE. In the remainder of this chapter I briefly present some simple analytical results that can be obtained from the LLE, and then discuss these two types of comb outputs. This discussion provides context for the results presented in the next two chapters. Fig. 1.4 summarizes the results that will be presented in the

remainder of this chapter, and in particular shows the values of the parameters α and F^2 at which solitons and extended patterns can be obtained.

1.2.1.1 Numerical simulation of the Lugiato-Lefever equation

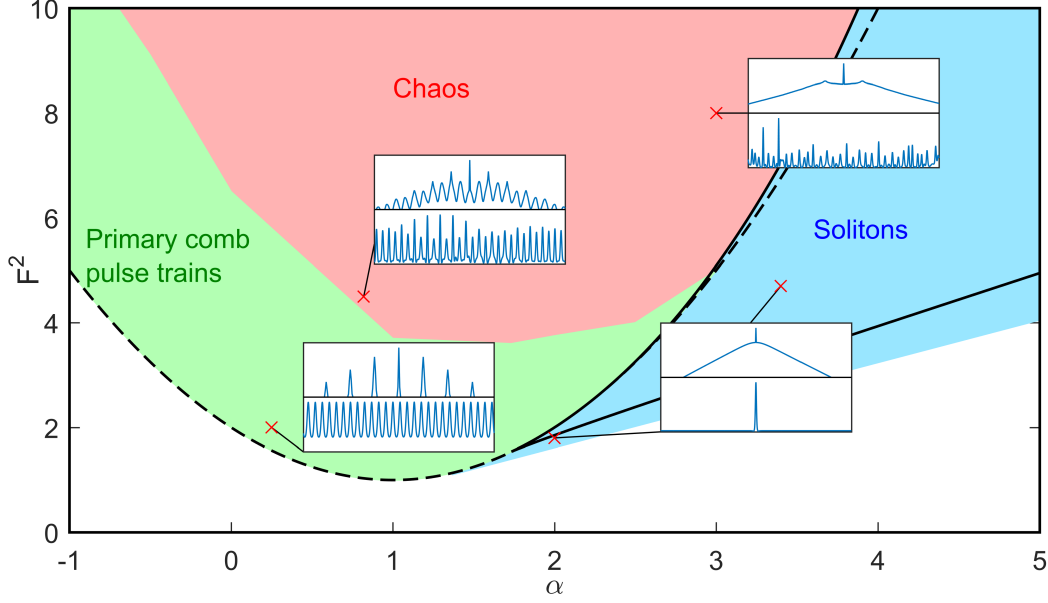


Figure 1.4: **Solution space for the Lugiato-Lefever equation.** Depiction of the various behaviors exhibited by ψ as a function of its position in the $\alpha - F^2$ plane; this predicts the type of Kerr-comb output as a function of the pump-laser detuning and power, the parameters that are most readily adjusted in experiment. Curves plotted in black are obtained through analytical investigation of the LLE; these include the threshold curve for parametric oscillation (dashed black, Eq. 1.18) and the lines obtained via $\rho(\alpha, F^2) = \rho_{\pm}(\alpha)$ (solid black, Eq. 1.16), which define the region where the LLE exhibits multiple flat solutions (i.e. solutions such that $\partial\psi/\partial\theta = 0$, Eq. 1.13). Extended patterns arise above the threshold curve through modulation instability. Solitons exist outside of the threshold curve at higher red detuning, up to an approximate maximum $\alpha_{max} = \pi^2 F^2/8$. The lines bounding the existence of chaos are not known precisely, and in fact chaos can be observed in simulation outside of the threshold curve at values $\alpha > \alpha_{thresh,+}$ (Eq. 1.19). Insets show representative simulation results for the various types of comb outputs in the frequency (top) and time (bottom) domains. Fig. after Ref. [31].

1.2.2 Analytical investigation of the resonator's CW response

Some insight into comb dynamics can be obtained via analytical investigations of the LLE, Eq. 1.11. This section largely follows the analysis of Ref. [31], with similar analysis having been performed elsewhere, for example in Refs. [27] and [32]. When the derivative term $\partial^2\psi/\partial\theta^2$ in the LLE is non-zero, ψ is necessarily broadband, and a Kerr comb has been formed. There are no known exact analytical solutions to the LLE to describe Kerr-comb outputs, which must instead be numerically simulated (see App. A). However, flat solutions ψ_s to the LLE may be calculated by setting all derivatives to zero—when these solutions can be realized physically (discussed below), they describe the behavior of the CW field that exists in the resonator in the absence of Kerr-comb formation. Upon setting the derivatives in the LLE to zero, one finds:

$$F = (1 + i\alpha)\psi_s - i|\psi_s|^2\psi_s. \quad (1.13)$$

The circulating intensity $\rho = |\psi_s|^2$ is obtained by taking the modulus-square of Eq. 1.13 to obtain:

$$F^2 = (1 + (\alpha - \rho)^2) \rho, \quad (1.14)$$

$$= \rho^3 - 2\alpha\rho^2 + (\alpha^2 + 1)\rho, \quad (1.15)$$

whereupon this equation can be numerically solved for ρ . As a third-order polynomial in ρ this equation has three solutions, one or three of which may be real; the complex solutions are unphysical. With α held constant, the function $F_\alpha^2(\rho)$ defined by this equation uniquely determines F^2 for a given value of ρ . By noting that $F^2(\rho = 0) = 0$ and $\partial F^2 / \partial \rho|_{\rho=0} > 0$, one can conclude that three real solutions for the inverted function $\rho_\alpha(F^2)$ exist between the values ρ_\pm that extremize $F_\alpha^2(\rho)$ when they are real:

$$\rho_\pm = \frac{2\alpha \pm \sqrt{\alpha^2 - 3}}{3}. \quad (1.16)$$

Outside of this interval there is only one real solution ρ . This is illustrated in Fig. 1.5. The smallest value of F^2 at which the stationary curve ρ becomes multivalued is found to be $F^2 = 8\sqrt{3}/9$ by solving for $\rho_- = \rho_+$ and inserting the corresponding values into Eq. 1.14.

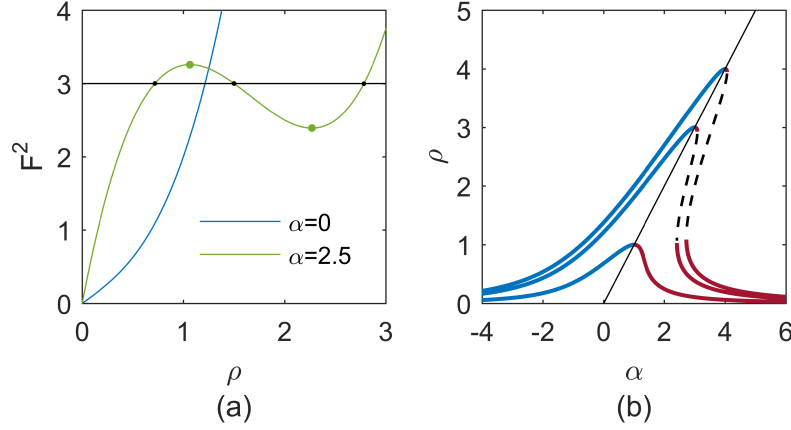


Figure 1.5: Investigation of the circulating CW power in a Kerr resonator. (a) Plots of F^2 as a function of ρ for $\alpha = 0$ (blue) and $\alpha = 2.5$ (green), according to Eq. 1.14. When real values of ρ exist that extremize F^2 according to this equation, multiple real solutions for the circulating power ρ (shown as black dots in this example) exist between these extremal values of F^2 (shown as green dots in this example). (b) Kerr-tilted resonances curves $\rho(\alpha)$ for $F^2 = 1$ (smallest), $F^2 = 3$, and $F^2 = 4$ (largest). The line $\rho = \alpha = F^2$ (solid black) marks the highest circulating power for a given input power F^2 and separates the effectively blue-detuned and effectively red-detuned branches. When $F^2 > 8\sqrt{3}/9$ (obtained by solving for $\rho_+ = \rho_-$, Eq. 1.16), the resonance becomes tilted steeply enough that an unstable middle branch (dashed black) exists.

Physically, the coexistence of multiple flat solutions ρ at a given point (α, F^2) corresponds to a ‘tilting’ of the Lorentzian transmission profile of the cavity and leads to bistability, even before taking into account thermal effects. This is illustrated in Fig. 1.5. For flat solutions ρ , an effective Kerr-shifted detuning can be defined as $\alpha_{eff} = \alpha - \rho$. The effective detuning simply incorporates the Kerr nonlinearity into the round-trip phase shift that describes the constructive or destructive interference of the circulating field with the pump at the coupling port. By noting that $\alpha = F^2 = \rho$ solves Eq. 1.14, we can conclude that the position of the effective Kerr-shifted resonance is on the line $\alpha = F^2$, where $\alpha_{eff} = 0$.

Once the circulating intensity ρ is known, the corresponding flat solution ψ_s can be determined

from Eq. 1.13 by inserting the known value of ρ and solving for ψ_s , with the result:

$$\psi_s = \frac{F}{1 + i(\alpha - \rho)}. \quad (1.17)$$

This expression reveals that the flat solution acquires a phase $\phi_s = \tan^{-1}(\rho - \alpha)$ relative to the pump.

If the flat solution(s) at a point (α, F^2) is (are) unstable, a Kerr comb will form spontaneously. Stability analysis of the flat solutions can be performed, and for the case of second-order dispersion alone the results are [31]:

- In the region of multi-stability, if the flat solutions are ordered with increasing magnitude as ρ_1 , ρ_2 , and ρ_3 , the middle solution ρ_2 is always unstable.
- When $\alpha < 2$, a flat solution ρ that is not the middle solution is stable if $\rho < 1$; otherwise it is unstable. When the flat solution is unstable, the mode that experiences the greatest instability has mode number $\mu_{max} = \sqrt{\frac{2}{\beta_2}}(\alpha - 2\rho)$.

Therefore, the pump-laser threshold curve for Kerr-comb generation can be determined in the $\alpha - F^2$ plane by setting $\rho = 1$ in Eq. 1.13:

$$F_{thresh}^2 = 1 + (\alpha - 1)^2, \quad (1.18)$$

$$\alpha_{thresh,\pm} = 1 \pm \sqrt{F^2 - 1}, \quad (1.19)$$

for an experiment in which the pump power or detuning is tuned while the other is held fixed.

1.2.3 Kerr comb outputs: extended modulation-instability patterns

Extended temporal patterns arise spontaneously as a result of the instability of the flat solution to the LLE when the pump laser is tuned above the threshold curve. Two types of extended patterns are shown in Fig. 1.6. These patterns can be stationary, in which case they are typically referred to as ‘Turing patterns’ or ‘primary comb,’ or can evolve in time, in which case they are typically referred to as ‘noisy comb’ or ‘spatiotemporal chaos.’ In general, the former occurs for lower values of the detuning α and smaller pump strengths F^2 ; although some studies of the transition from Turing patterns to chaos have been conducted (e.g. Ref. [33]), a well-defined boundary between the two has not been established, and may not exist.

In the spatial domain parametrized by θ , a Turing pattern consists of a pulse train with (typically) $n \gg 1$ pulses in the domain $-\pi \leq \theta \leq \pi$ —the pulse train’s repetition rate is a multiple of the cavity FSR: $f_{rep} = n \times f_{FSR}$. Corresponding to the n -fold decreased period (relative to the round-trip time) of an n -pulse Turing pattern’s modulated waveform in the time domain, the optical spectrum of a Turing pattern consists of modes spaced by n resonator FSR—it is this widely-spaced spectrum that is referred to as ‘primary comb.’ Analytical approximations for Turing patterns are possible near threshold [34, 35] and in the small damping limit [36]. The stability analysis results from the last section can be used to predict the spacing n of a primary comb (equivalently the number of Turing-pattern pulses) generated in a decreasing-frequency scan across the resonance with fixed normalized pump power F^2 : $n = \mu_{max,thresh} = \sqrt{\Delta\omega_0(1 + \sqrt{F^2 - 1})/D_2}$. Fig. 1.6a shows measured and simulated primary comb spectra and Fig. 1.6b shows the corresponding simulated time-domain waveform.

Spatiotemporal chaos can be understood as a Turing pattern whose pulses oscillate in height, with adjacent pulses oscillating out of phase. From such an oscillating Turing pattern, if α and/or F^2 is increased, one moves deeper into the chaotic regime and pulses begin to exhibit lateral motion and collisions; the number of pulses present in the cavity is no longer constant in time. Depending on the severity of the chaos (greater for larger α and F^2), a chaotic comb may correspond to a primary-comb-type spectrum with each primary-comb mode exhibiting sidebands at the resonator

FSR, so-called ‘subcombs,’ or it may correspond to a spectrum with light in each cavity mode. Fig. 1.6c shows measured and simulated time-averaged spectra of chaotic combs and Fig. 1.6d shows a corresponding simulated time-domain waveform.

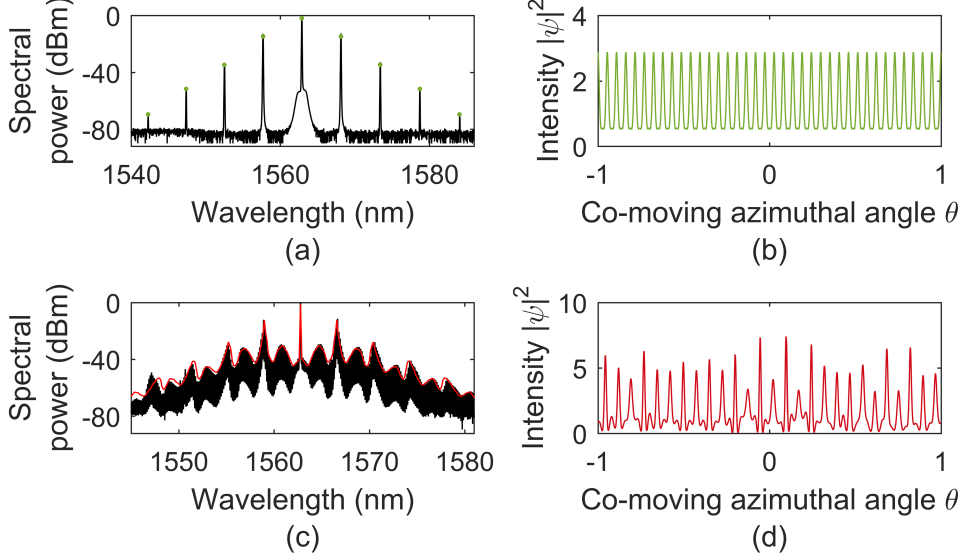


Figure 1.6: **Extended-pattern solutions to the LLE.** (a,b) Primary-comb pulse train in the frequency (a) and time (b) domains. The primary-comb spectrum corresponds to 39 time-domain pulses. The experimental optical spectrum (black) was obtained in a microdisk resonator with 17.32 GHz free-spectral range, and the simulation (green) is conducted with parameters near typical experimental values: $F^2=6$, $\alpha = -0.6$, and $\beta_2 = -0.0044$. (c,d) Spatiotemporal chaos obtained in the same resonator. The experimental measurement (black) yields a time-averaged optical spectrum, with a simulation of qualitatively similar dynamics shown in red. Simulation parameters are $F^2 = 4.2$, $\alpha = 1.2$, and $\beta_2 = -0.0054$. A snapshot of the evolving time-domain waveform is shown in (d).

Relative to generation of solitons, discussed below, experimental generation of an extended pattern is straightforward. These patterns are generated with blue effective pump-laser detuning $\alpha_{eff} < 0$, where thermal locking can occur. Because they arise spontaneously from noise, their generation is (comparatively) straightforward: simply decrease the pump-laser frequency until a pattern is generated. Unfortunately, operation of a Kerr-comb in the extended pattern regime is disadvantageous for applications: the n -FSR spacing of primary comb presents a challenge for measurement of the repetition rate of the frequency comb due to the bandwidth of measurement electronics and is also an inefficient use of physical space (i.e. for an n -pulse primary comb pulse train, an equivalent pulse train can always be obtained using the single-soliton output of a resonator with area that is smaller by a factor of $1/n^2$), and the aperiodic time-evolution of chaotic comb corresponds to modulation sidebands on the comb modes within the linewidth of the cavity that preclude the use of the comb as a set of stable optical reference frequencies.

An important property of these extended patterns is that they fill the resonator—the characteristic size of temporal features scales roughly as $1/\sqrt{-\beta_2}$, but these features are distributed densely and uniformly throughout the resonator. This means that the total circulating power of an extended pattern $\int d\theta |\psi|^2$ is large relative to the localized pulses discussed in the next section, and therefore that extended patterns come with a comparatively large thermal shift of the resonance.

1.2.4 Kerr comb outputs: solitons

The term ‘soliton’ generally refers to a localized excitation that can propagate without changing its shape due to a delicate balance between dispersion (or diffraction) and nonlinearity. Solitons are found in several contexts within the field of nonlinear optics, and temporal Kerr-soliton pulses in optical fibers are particularly well known. Microresonators support so-called dissipative cavity solitons, which are localized pulses circulating the resonator that are out-coupled once per round trip. In the case of a single circulating soliton, this leads to a train of pulses propagating away from the resonator with repetition rate $1/T_{RT}$. Thus the mode spacing of the comb matches the FSR of the resonator, in contrast with widely-spaced primary comb spectra, and the soliton can, in principle, remain stable and propagate indefinitely as a stationary solution to the LLE. This makes Kerr combs based on solitons particularly attractive for applications.

1.2.4.1 Mathematical description of solitons

Solitons in optical fibers are solutions of the nonlinear Schrodinger equation (NLSE) that describes pulse-propagation in optical fiber [8]:

$$\frac{\partial A}{\partial z} = i\gamma|A|^2 A - i\frac{\beta}{2}\frac{\partial^2 A}{\partial T^2}. \quad (1.20)$$

This equation describes the evolution of the pulse envelope A in the ‘fast-time’ reference frame parametrized by T as it propagates down the length of the fiber, parametrized by the distance variable z . Here γ is the nonlinear coefficient of the fiber and $\beta \equiv \beta_{prop,2}$ is the GVD parameter. The LLE can be viewed as an NLSE with additional loss and detuning terms $-(1 + i\alpha)\psi$ and a driving term F .

The fundamental soliton solution to the NLSE is:

$$A_{sol} = \sqrt{P_0} \operatorname{sech}(T/\tau) e^{i\gamma P_0 z/2 + i\phi_0}, \quad (1.21)$$

where P_0 is the peak power of the pulse and is related to the duration of the pulse τ via $\tau = \sqrt{-\beta/\gamma P_0}$, and ϕ_0 is an arbitrary phase. Thus, this equation admits a *continuum* of pulsed fundamental ‘soliton’ solutions, with one existing for each value of the peak power. Each of these solutions propagates down the fiber without changing shape; only the phase evolves with distance as $\phi(z) = \gamma P_0 z/2 + \phi_0$.

The introduction of the loss, detuning, and driving terms into the NLSE to obtain the LLE has several important consequences for solitons. First, exact analytical expressions for the soliton solution to the LLE in terms of elementary functions are not known, in contrast with the situation for the NLSE. However, the soliton solutions to the LLE, Eq. 1.11, can be approximated well as:

$$\psi_{sol} = \psi_{s,min} + e^{i\phi_0} \sqrt{2\alpha} \operatorname{sech} \sqrt{\frac{2\alpha}{-\beta_2}} \theta. \quad (1.22)$$

Here $\psi_{s,min}$ is the flat solution to the LLE from Eq. 1.17 at the point where the soliton solution is desired; when multiple flat solutions exist, $\psi_{s,min}$ is the one corresponding to the smallest intensity ρ_1 . The phase $\phi_0 = \cos^{-1}(\sqrt{8\alpha}/\pi F)$ arises from the intensity-dependent phase shift in the cavity due to the Kerr effect, mathematically described by the term $i|\psi|^2\psi$. We depict this approximation, alongside numerical calculations of exact soliton solutions to the LLE, in Fig. 1.7.

This approximation ψ_{sol} from Eq. 1.22 for the soliton solution of the LLE illustrates a second important consequence of the differences between the NLSE and the LLE: while the NLSE admits a continuum of fundamental soliton solutions parametrized by their peak power P_0 and arbitrary phase ϕ_0 , the LLE supports only one shape for the envelope of a soliton for fixed experimental parameters. Intuitively, this can be understood as arising from the need for the round-trip phase shift for all points on the soliton to be zero in steady-state; the introduction of the detuning parameter α breaks the degeneracy that exists for the NLSE within the continuum of soliton solutions.

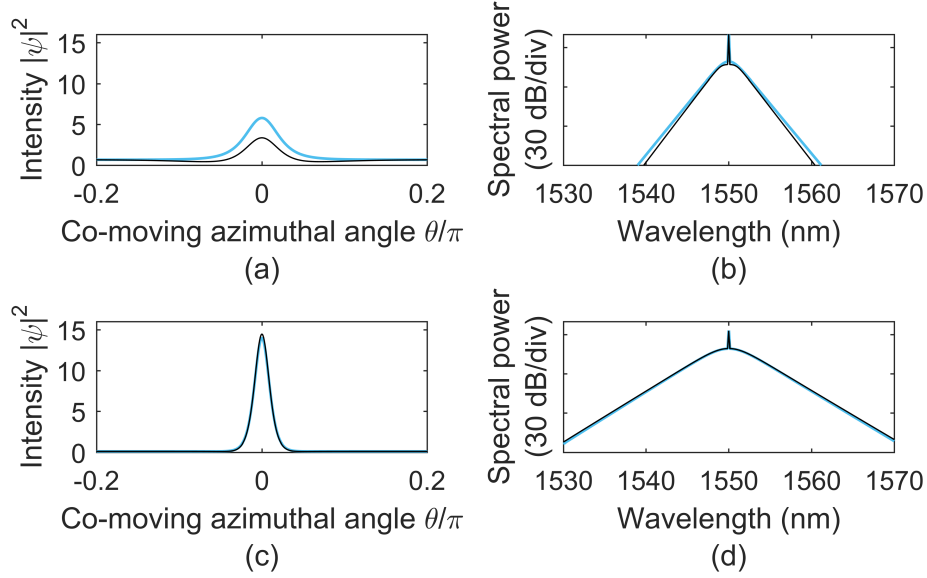


Figure 1.7: **Soliton solutions to the LLE.** Analytical approximations (color) and numerically-calculated exact solutions (black) to the LLE in the time (a,c) and frequency (b,d) domains. The solitons are calculated at $\alpha = 0.95 \alpha_{max} = \pi^2 F^2 / 8$ for $F^2 = 8\sqrt{3}/9$ (a,b) and $F^2 = 6$ (c,d) with $\beta_2 = -0.02$ in both cases. The isolated spectral spike is at the pump frequency and corresponds to the CW background $\psi_{s,min}$. Spectra are calculated using $f_{rep} = 16.5$ GHz with pump wavelength of $\lambda_p = 1550$ nm. For experimental measurements of solitons in microring resonators, see Chapters ?? and ??.

The analytical approximation in Eq. 1.22 indicates the scaling of the amplitude and width of the LLE soliton with the experimental parameters: the amplitude of the LLE soliton, prior to its summation with the CW background, depends only on the detuning α , and the width of the soliton increases with larger detuning α and smaller dispersion β_2 . Importantly, if one is concerned with maximizing the bandwidth of the soliton, it is important to minimize β_2 and maximize α , due to the inverse relationship between temporal duration and spectral bandwidth. The spectrum of a single-soliton Kerr comb has a $\text{sech}^2((\omega - \omega_p)/\Delta\omega_{sol})$ envelope, where ω is the optical angular frequency and $\Delta\omega_{sol} \approx \sqrt{32\alpha/|\beta_2|T_{RT}^2}$ is the bandwidth of the pulse in angular frequency. Equivalently, the bandwidth of the soliton in (linear) optical frequency is $\sqrt{\frac{16\Delta\nu f_{rep}^2}{D_2}\alpha}$; the spectral width in mode number is $\Delta\mu_{sol} \approx 4\sqrt{\alpha\delta\nu/D_2}$. Consistent with the phase ϕ_0 in the approximation ψ_{sol} in Eq. 1.22, solitons can exist up to a maximum detuning of $\alpha_{max} \sim \pi^2 F^2 / 8$ [23]. For a soliton at the maximum detuning for fixed normalized pump power F^2 , the bandwidth is then $\sqrt{\frac{\pi^2 \Delta\nu f_{rep}^2}{2D_2} F^2}$.

Solitons exist only where there is a stable flat solution ψ_s that is effectively red detuned that can form the background for the pulse [32, 37]. This effectively red-detuned background is itself thermally unstable (see Sec. 1.1.2), but the existence of the soliton acts to stabilize the pump detuning. As explained by Herr et al., the soliton provides a local modulation of the refractive index through the Kerr effect, which changes the round-trip phase shift of pump light that arrives coincidentally with the soliton at the coupling port [23]. This leads to a *local* increase in the resonant wavelength for this pump light. Thus there are effectively two resonant wavelengths, a smaller one determined by the round-trip phase shift including the Kerr shift from the CW background, and a larger one determined by the round-trip phase shift including the Kerr shift from the soliton. The pump laser can be effectively blue-detuned with respect to the latter resonance, which can lead to

thermally stable operation in the soliton regime.

Solitons are strongly localized: as can be seen from Eq. 1.22, the deviation of the background intensity from ρ_1 near a soliton at θ_0 is proportional to $e^{-(\theta-\theta_0)/\delta\theta}$, where $\delta\theta = \sqrt{-\beta_2/2\alpha}$. If $\delta\theta$ is sufficiently small, multiple solitons can be supported in the resonator domain $-\pi \leq \theta \leq \pi$ with negligible interactions between solitons. Simulations reveal that if $(\theta - \theta_0)/\delta\theta$ is too small, solitons exhibit attractive interactions; the result of this attraction can be pair-wise annihilation or pair-wise merger, with the ultimate result being an ensemble with fewer solitons. The maximum number of solitons that can coexist in a resonator in the absence of higher-order stabilizing effects (see Chapter ?? and Refs. [38, 39]) can be approximated as $N_{max} \approx \sqrt{-2/\beta_2}$ [23]. An approximation to the form of a soliton ensemble is possible as:

$$\psi_{ens} = \psi_{s,min} + e^{i\phi_0} \sqrt{2\alpha} \sum_j \operatorname{sech} \left(\sqrt{\frac{2\alpha}{-\beta_2}} (\theta - \theta_j) \right), \quad (1.23)$$

where $\{\theta_j\}$ define the positions of the solitons in the ensemble and $\phi_0 = \cos^{-1}(\sqrt{8\alpha}/\pi F)$ as above. Fig. 1.8 provides an example illustrating the degeneracy in soliton number of Kerr-combs operating in the soliton regime.

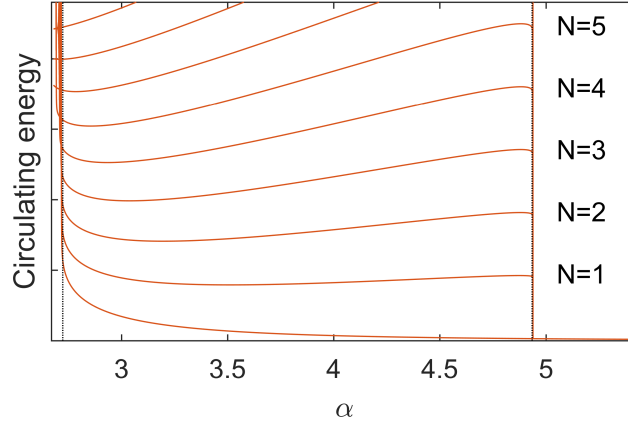


Figure 1.8: **Kerr-soliton energy-level diagram.** Some of the possible values of the circulating energy (proportional to $\int d\theta |\psi|^2$) in the soliton regime as a function of the detuning parameter α . Level curves correspond to the number of circulating solitons. This diagram is obtained from numerical solutions using $F^2 = 4$, $\beta_2 = -0.0187$, and is quantitatively dependent on both of these parameters. Dotted vertical lines indicate approximations to the minimum and maximum detunings for solitons. The approximation for the minimum detuning is the value of α at which the effectively red-detuned branch vanishes, obtained by inserting ρ_- (Eq. 1.16) into Eq. 1.14 for $F^2 = 4$ and solving for α , and the approximate maximum detuning is $\alpha_{max} = \pi^2 F^2 / 8$.

1.2.4.2 Microresonator solitons in experiments

Relative to the generation of extended modulation-instability patterns, experimental generation of solitons in microring resonators is challenging. Solitons are localized excitations below threshold, which means that their existence is degenerate with their absence—a resonator can host $N = 0, 1, 2, \dots$ up to N_{max} solitons for a given set of parameters α and F^2 ; as discussed above and illustrated in Fig. 1.8. If α and F^2 are experimentally tuned to a point at which solitons may exist, ψ will evolve to a form determined by the initial conditions of the field ψ . To provide initial conditions that evolve to $N > 0$ solitons, most experimental demonstrations of soliton generation have involved

first generating an extended pattern in the resonator, and then tuning to an appropriate point (α, F^2) so that ‘condensation’ of solitons from the extended pattern occurs.

Condensation of solitons from an extended pattern presents additional challenges. First, it is difficult to control the number of solitons that emerge, due to the high degree of soliton-number degeneracy as shown in Fig. 1.8. This typically leads to a success rate somewhat lower than 100 % in the generation of single solitons. Second, the transition from a high duty-cycle extended pattern to a lower duty-cycle ensemble of one or several solitons comes with a dramatic drop in intracavity power that occurs on the timescale of the photon lifetime. If the resonator is in thermal steady-state before this drop occurs, the resonator will cool and the resonance frequency will increase. If this increase is large enough that the final detuning α exceeds $\alpha_{max} = \pi^2 F^2/8$, the soliton is lost. This challenge can be addressed by preparing initial conditions for soliton generation and then tuning to an appropriate point (α, F^2) faster than the cavity can come into thermal steady-state at the temperature determined by the larger power of the extended pattern; this is possible because the timescale over which an extended pattern can be generated is related to the photon lifetime, which is typically much faster than the thermal timescale.

The first report of soliton generation in microresonators came in 2012 in a paper by Herr et al. [23] (2012 pre-print [22]). These authors described optimizing the speed of a decreasing-frequency scan of the pump laser across the cavity resonance so that solitons could be condensed from an extended pattern and the scan could then be halted at a laser frequency where the solitons could be maintained with the system in thermal steady-state at the temperature determined by the circulating power of the solitons. Stochastic reduction in the number of solitons in the resonator after condensation from an extended pattern was identified in these experiments. This corresponds to transitions between levels in the diagram in Fig. 1.8, and is associated with discrete steps in a measurement of the ‘comb power,’ the output power of the resonator with the pump frequency ν_p filtered out. The resulting staircase-like nature of a comb power measurement is a useful experimental signature of soliton generation in microresonators, and is important for comparison with the results described in Chapter ??.

Other approaches for dealing with the challenges described above have been developed since this first demonstration; these include fast manipulation of the pump power [40, 41], periodic modulation of the pump laser’s phase or power at f_{FSR} [5, 42], tuning of the cavity resonance frequency using chip-integrated heaters instead of tuning the pump-laser frequency [43, 44], and soliton-ensemble preparation and subsequent population reduction through manipulation of the pump laser [45]. These methods continue to make use of extended patterns to provide initial conditions for soliton generation. In formally-equivalent fiber-ring resonators, direct generation of solitons without condensation from an extended pattern has been demonstrated using transient phase and/or amplitude modulation of the pump laser [46–48].

1.2.4.3 Microresonator solitons in applications

Because solitons have single-FSR spacing, have the output localized into a high peak-power pulse, and are stationary (in contrast with chaos, which has single-FSR spacing but is not stationary), they are promising for applications. Many of the proposals for and demonstrations of applications with Kerr-combs have used single-soliton operation. Some of the applications already demonstrated include an optical clock [49], dual-comb spectroscopy [50], coherent communications [51], and direct on-chip optical frequency synthesis [52]. Additionally, soliton combs have been self-referenced both with [53, 54] and without [55, 56] external spectral broadening. Nevertheless, there remains work to be done to bring microresonator-soliton technology to the level of maturity that will be required for deployment in the field. Chapters ?? and ?? describe two recent advancements: the development of a method for direct on-demand generation of single solitons by use of a phase-modulated pump laser, and the observation and explanation of a soliton-interaction mechanism that imparts rigid structure on the allowed configurations of multi-soliton ensembles.

Appendix A

Numerical simulations of nonlinear optics

This appendix describes the algorithm used for numerical simulation of the generalized nonlinear Schrodinger equation (GNLSE) and Lugiato-Lefever equation (LLE) to obtain the results presented in the preceding chapters in this thesis. These equations are simulated with Matlab using a fourth-order Runge-Kutta interaction picture (RK4IP) method [57] with adaptive step size [58]. The RK4IP method is a particular algorithm in the broader class of split-step Fourier algorithms in which nonlinearity is implemented in the time domain and dispersion is implemented in the frequency domain. An illustrative example of the split-step Fourier approach is a far simpler algorithm carried out with a single line of Matlab code to simulate the LLE:

```
psi=ifft(exp(delta*L).*fft(exp(delta*(1i*abs(psi).^2+F./psi)).*psi));
```

where δ is the step size and L is a linear frequency-domain dispersion operator (\hat{L} , see below) that has been defined in the preceding code. The RK4IP algorithm with adaptive step size is advantageous over this simple algorithm in calculation time and in the scaling of error with the step size.

A.1 RK4IP algorithm

The LLE (NLSE) describes the evolution of the field $\psi(A)$, a function of a fast variable $\theta(T)$, over a timescale parametrized by a slow variable $\tau(z)$. In what immediately follows we use the variable names corresponding to the LLE for simplicity. Each of these equations can be written as the sum of a nonlinear operator \hat{N} and a linear operator \hat{L} acting on ψ , so that the field ψ evolves as

$$\frac{\partial \psi}{\partial \tau} = (\hat{N} + \hat{L})\psi, \quad (\text{A.1})$$

which can be implemented with the split-step Fourier approach.

The RK4IP algorithm specifies a recipe for advancing the field a single step δ in the slow variable τ to obtain $\psi(\theta, \tau + \delta)$ from $\psi(\theta, \tau)$. This specific algorithm has the attractive feature that it reduces the number of Fourier transformations that must be performed to achieve a given

calculation accuracy relative to other common algorithms. The RK4IP algorithm is [57]:

$$\psi_I = \exp\left(\frac{\delta}{2}\hat{L}\right)\psi(\theta, \tau) \quad (\text{A.2})$$

$$k_1 = \exp\left(\frac{\delta}{2}\hat{L}\right)\left[\delta\tau\hat{N}(\psi(\theta, \tau))\right]\psi(\theta, \tau) \quad (\text{A.3})$$

$$k_2 = \delta\hat{N}(\psi_I + k_1/2)[\psi_I + k_1/2] \quad (\text{A.4})$$

$$k_3 = \delta\hat{N}(\psi_I + k_2/2)[\psi_I + k_2/2] \quad (\text{A.5})$$

$$k_4 = \delta\hat{N}\left(\exp\left(\frac{\delta}{2}\hat{L}\right)(\psi_I + k_3)\right) \quad (\text{A.6})$$

$$\times \exp\left(\frac{\delta}{2}\hat{L}\right)(\psi_I + k_3) \quad (\text{A.7})$$

$$\psi(\theta, \tau + \delta) = \exp\left(\frac{\delta}{2}\hat{L}\right)[\psi_I + k_1/6 + k_2/3 + k_3/3] + k_4/6. \quad (\text{A.8})$$

In the above it is understood that \hat{L} is applied in the frequency domain and \hat{N} is applied in the time domain. Calculation of $\psi(\theta, \tau + \delta)$ from $\psi(\theta, \tau)$ therefore requires eight Fourier transformations.

A.2 Adaptive step-size algorithm

An adaptive step-size algorithm is a strategy for adjusting the magnitude of the steps δ that are taken to optimize the simulation speed while maintaining a desired degree of accuracy. The RK4IP algorithm exhibits error that scales locally as $O(\delta^5)$. Since reducing the step size naturally requires more steps and therefore increases the number of small errors that accumulate, the resulting global accuracy of the algorithm is $O(\delta^4)$. One appropriate step-size adjustment algorithm for this scaling is described by Heidt [58]. For a given goal error e_G , the algorithm goes as follows:

- Calculate a field ψ_{coarse} by advancing the field $\psi(\theta, \tau)$ according to RK4IP by a step of size δ .
- Calculate a field ψ_{fine} by advancing the field $\psi(\theta, \tau)$ according to RK4IP by two steps of size $\delta/2$.
- Calculate the measured error $e = \sqrt{\sum_j |\psi_{coarse,j} - \psi_{fine,j}|^2 / \sum_j |\psi_{fine,j}|^2}$, where j indexes over the discrete points parametrizing the fast variable θ .
 - * If $e > 2e_G$, discard the solution and repeat the process with coarse step size $\delta' = \delta/2$.
 - * If $e_G < e < 2e_G$, the evolution continues and the step size is reduced to $\delta' = \delta/2^{1/5} \approx 0.87\delta$.
 - * If $e_G/2 < e < e_G$, the evolution continues and the step size is not changed.
 - * If $e < e_G/2$, the evolution continues and the step size is increased to $\delta' = 2^{1/5}\delta \approx 1.15\delta$.

When the simulation continues, the new field $\psi(\theta, \tau + \delta)$ is taken to be $\psi(\theta, \tau + \delta) = 16\psi_{fine}/15 - \psi_{coarse}/15$. In the calculations described in this thesis, the goal error e_G is typically 10^{-6} .

A.3 Pseudocode for numerical simulation with the RK4IP algorithm and adaptive step size

The pseudocode shown in Algorithm 1 shows how the RK4IP algorithm with adaptive step size is implemented. This pseudocode neglects the specific details of the RK4IP algorithm.

Two notes:

- The current field $\psi(\theta, \tau)$ is stored until the approximation to the new field $\psi(\theta, \tau + \delta)$ is found to be acceptable.
- This implementation makes use of an extra efficiency that is possible when the solution is discarded and the step size is halved: the first step of the fine solution $\psi_{fine,1}$ for the previous attempt becomes the coarse solution ψ_{coarse} for the current attempt.

Algorithm 1 Pseudocode showing the implementation of RK4IP with adaptive step size.

```

procedure
  while  $\tau < \tau_{end}$  do
     $e = 1$  ▷ Initialize the error to a large value
     $firsttry = TRUE$  ▷ For more efficiency if this is not the first attempt (see below)
     $\delta = 2\delta$  ▷ To account for halving on the first iteration

    while  $e > 2e_G$  do
      if  $firsttry$  then
         $\psi_{coarse} = \text{RK4IP}(\psi, \delta)$ 
      else
         $\psi_{coarse} = \psi_{fine,1}$  ▷ We get to re-use the first step of the previous attempt's fine solution

       $\delta = \delta/2$ 
       $\psi_{fine} = \psi$ 

      for  $j_{step} = 1 : 2$  do
         $\psi_{fine} = \text{RK4IP}(\psi_{fine}, \delta)$ 
        if  $j_{step} = 1$  then
           $\psi_{fine,1} = \psi_{fine}$ 

       $e = \sqrt{\sum |\psi_{coarse} - \psi_{fine}|^2 / \sum |\psi_{fine}|^2}$ 
       $firsttry = FALSE$ 

       $\psi = 16\psi_{fine}/15 - \psi_{coarse}/15$ 
       $\tau = \tau + 2\delta$  ▷ We took two fine steps of size  $\delta$ 

    if  $e > e_G$  then
       $\delta = \delta/2^{1/5}$ 
    if  $e < e_G/2$  then
       $\delta = 2^{1/5}\delta$ 

```

A.3.1 Simulation of the LLE

For simulation of the LLE, the operators are:

$$\hat{N} = i|\psi|^2 + F/\psi, \quad (\text{A.9})$$

$$\hat{L} = -(1 + i\alpha_\mu), \text{ where} \quad (\text{A.10})$$

$$\alpha_\mu = \alpha - \sum_{n=1}^N \beta_n \mu^n / n!. \quad (\text{A.11})$$

The subscript μ indicates the pump-referenced mode number upon which the operator acts. Note, in particular, that the pump term F has been incorporated into the nonlinear operator, so that it is implemented in the time domain. The quantity $\hat{N}\psi$ then becomes $i|\psi|^2\psi + F$, as required for computation of $\partial\psi/\partial\tau$.

A.3.2 Simulation of the GNLSE

The GNLSE used in the simulations conducted for Chapter ?? contains nonlinear terms that describe the medium's Raman response and self-steepening. The equation employed can be written

as [8, 57]:

$$\begin{aligned} \frac{\partial A}{\partial z} = & - \left(\sum_n \beta_n \frac{i^{n-1}}{n!} \frac{\partial^n}{\partial T^n} \right) A + i\gamma \left(1 + \frac{1}{\omega_0} \frac{\partial}{\partial T} \right) \\ & \times \left((1 - f_R)A|A|^2 + f_RA \int_0^\infty h_R(\tau)|A(z, T - \tau)|^2 d\tau \right). \end{aligned} \quad (\text{A.12})$$

For Chapter ??, second- and third-order dispersion is used with $\beta_2 = -7.7 \text{ ps}^2/\text{km}$ and $\beta_3 = 0.055 \text{ ps}^3/\text{km}$, where β_n is the n^{th} frequency-derivative of the propagation constant. The nonlinear coefficient $\gamma = \frac{2\pi}{\lambda} \frac{n_2}{A_{eff}}$ used is 11 W/km [59], coming from an effective mode-field diameter of $\sim 3.5 \mu\text{m}$ for the HNLF used in the experiment and the nonlinear index $n_2 = 2.7 \times 10^{-16} \text{ cm}^2/\text{W}$ of silica. The quantity $\omega_0 = 2\pi c/\lambda_0$ is the (angular) carrier frequency of the pulse, and the parameter $f_R = 0.18$ and function

$$h_R(\tau > 0) = (\tau_1^2 + \tau_2^2)/(\tau_1\tau_2^2) \times e^{-\tau/\tau_2} \sin \tau/\tau_1 \quad (\text{A.13})$$

describe the medium's Raman response, with $\tau_1 = 12.2 \text{ fs}$ and $\tau_2 = 32 \text{ fs}$ used here [8, 57, 60].

The linear frequency-domain operator applied in the RK4IP algorithm is

$$\hat{L} = i\frac{\beta_2}{2}(\omega_\mu - \omega_0)^2 - \frac{\beta_3}{6}(\omega_\mu - \omega_0)^3 \quad (\text{A.14})$$

Here ω_μ is defined by the discretization of the frequency domain due to Fourier-transformation of a finite temporal window of length T_{comp} via $\omega_\mu = \omega_0 + 2\pi\mu/T_{comp}$; where T_{comp} is the size of the domain for the fast time variable T .

The nonlinear operator \hat{N} for the GNLSE implements the convolution as a product in the frequency domain. That is,

$$\hat{N} = i\gamma \frac{1}{A} \left(1 + \frac{1}{\omega_0} \frac{\partial}{\partial T} \right) \times \left[(1 - f_R)A|A|^2 + f_RA \mathcal{F}^{-1} \{ \chi_R \cdot \mathcal{F}(|A|^2) \} \right], \quad (\text{A.15})$$

where $\chi_R = \mathcal{F}\{h_R(\tau)\}$ and \mathcal{F} denotes Fourier transformation. Procedurally, the quantity in the square brackets is calculated first, and then the fast-time derivative is implemented and the sum in the curved brackets is calculated.

References

- [1] T. J. Kippenberg, R. Holzwarth, and S. A. Diddams. Microresonator-Based Optical Frequency Combs. *Science (New York, N.Y.)*, 332 (6029), **2011**, 555–559. DOI: 10.1126/science.1193968 (cited on pages 1, 6).
- [2] A. A. Savchenkov, A. B. Matsko, and L. Maleki. On Frequency Combs in Monolithic Resonators. *Nanophotonics*, 5, **2016**, 363–391. DOI: 10.1515/nanoph-2016-0031 (cited on page 1).
- [3] Y. K. Chembo. Kerr optical frequency combs: Theory, applications and perspectives. *Nanophotonics*, 5 (2), **2016**, 214–230. DOI: 10.1515/nanoph-2016-0013 (cited on page 1).
- [4] A. Pasquazi, M. Peccianti, L. Razzari, D. J. Moss, S. Coen, M. Erkintalo, Y. K. Chembo, T. Hansson, S. Wabnitz, P. Del’Haye, X. Xue, A. M. Weiner, and R. Morandotti. Micro-combs: A novel generation of optical sources. *Physics Reports*, 729, **2017**, 1–81. DOI: 10.1016/j.physrep.2017.08.004 (cited on page 1).
- [5] E. Obrzud, S. Lecomte, and T. Herr. Temporal solitons in microresonators driven by optical pulses. *Nature Photonics*, 11 (August), **2017**, 600–607. DOI: 10.1038/nphoton.2017.140. arXiv: 1612.08993 (cited on pages 1, 15).
- [6] H. Lee, T. Chen, J. Li, K. Y. Yang, S. Jeon, O. Painter, and K. J. Vahala. Chemically etched ultrahigh-Q wedge-resonator on a silicon chip. *Nature Photonics*, 6 (6), **2012**, 369–373. DOI: 10.1038/nphoton.2012.109. arXiv: 1112.2196 (cited on page 2).
- [7] K. Y. Yang, K. Beha, D. C. Cole, X. Yi, P. Del’Haye, H. Lee, J. Li, D. Y. Oh, S. A. Diddams, S. B. Papp, and K. J. Vahala. Broadband dispersion-engineered microresonator on a chip. *Nature Photonics*, 10 (March), **2016**, 316–320. DOI: 10.1038/nphoton.2016.36 (cited on page 2).
- [8] G. P. Agrawal. **Nonlinear Fiber Optics**. 4th. Burlington, MA: Elsevier, 2007 (cited on pages 1, 5, 7, 12, 20).
- [9] M. L. Calvo and V. Lakshminarayanan, eds. **Optical Waveguides: From Theory to Applied Technologies**. Boca Raton, FL: Taylor & Francis, 2007 (cited on page 1).
- [10] P. Del’Haye, S. A. Diddams, and S. B. Papp. Laser-machined ultra-high-Q microrod resonators for nonlinear optics. *Applied Physics Letters*, 102, **2013**, 221119 (cited on page 2).
- [11] A. N. Oraevsky. Whispering-gallery waves. *Quantum Electronics*, 32 (42), **2002**, 377–400. DOI: 10.1070/QE2001v031n05ABEH002205. arXiv: arXiv:1011.1669v3 (cited on page 2).
- [12] H. A. Haus. **Waves and Fields in Optoelectronics**. Englewood Cliffs: Prentice-Hall, 1984 (cited on pages 2, 3).
- [13] S. M. Spillane, T. J. Kippenberg, O. J. Painter, and K. J. Vahala. Ideality in a Fiber-Taper-Coupled Microresonator System for Application to Cavity Quantum Electrodynamics. *Physical review letters*, 91 (4), **2003**, 043902. DOI: 10.1103/PhysRevLett.91.043902 (cited on page 3).
- [14] V. S. Il’chenko and M. L. Gorodetskii. Thermal nonlinear effects in optical whispering gallery microresonators.pdf. *Laser Physics*, 2 (6), **1992**, 1004–1009 (cited on page 4).

- [15] T. Carmon, L. Yang, and K. J. Vahala. Dynamical thermal behavior and thermal self-stability of microcavities. *Optics Express*, 12 (20), **2004**, 4742–4750. URL: <http://www.ncbi.nlm.nih.gov/pubmed/19484026><http://www.opticsinfobase.org/oe/abstract.cfm?uri=oe-12-20-4742> (cited on page 4).
- [16] R. W. Boyd. **Nonlinear Optics**. San Diego, CA: Elsevier, 2003 (cited on page 5).
- [17] R. del Coso and J. Solis. Relation between nonlinear refractive index and third-order susceptibility in absorbing media. *Journal of the Optical Society of America B*, 21 (3), **2004**, 640. DOI: 10.1364/JOSAB.21.000640 (cited on page 5).
- [18] P Del’Haye, A Schliesser, O Arcizet, T Wilken, R Holzwarth, and T. J. Kippenberg. Optical frequency comb generation from a monolithic microresonator. *Nature*, 450 (7173), **2007**, 1214–1217. DOI: 10.1038/nature06401 (cited on page 5).
- [19] T. Kippenberg, S. Spillane, and K. Vahala. Kerr-Nonlinearity Optical Parametric Oscillation in an Ultrahigh-Q Toroid Microcavity. *Physical Review Letters*, 93 (8), **2004**, 083904. DOI: 10.1103/PhysRevLett.93.083904 (cited on page 6).
- [20] A. A. Savchenkov, A. B. Matsko, D. Strekalov, M. Mohageg, V. S. Ilchenko, and L. Maleki. Low threshold optical oscillations in a whispering gallery mode CaF₂ resonator. *Physical Review Letters*, 93 (24), **2004**, 2–5. DOI: 10.1103/PhysRevLett.93.243905 (cited on page 6).
- [21] I. H. Agha, Y. Okawachi, M. A. Foster, J. E. Sharping, and A. L. Gaeta. Four-wave-mixing parametric oscillations in dispersion-compensated high-Q silica microspheres. *Physical Review A - Atomic, Molecular, and Optical Physics*, 76 (4), **2007**, 1–4. DOI: 10.1103/PhysRevA.76.043837 (cited on page 6).
- [22] T. Herr, V. Brasch, J. D. Jost, C. Y. Wang, N. M. Kondratiev, M. L. Gorodetsky, and T. J. Kippenberg. Temporal solitons in optical microresonators. *arXiv*, **2012**, 1211.0733. DOI: 10.1038/nphoton.2013.343. arXiv: 1211.0733 (cited on pages 6, 15).
- [23] T. Herr, V. Brasch, J. D. Jost, C. Y. Wang, N. M. Kondratiev, M. L. Gorodetsky, and T. J. Kippenberg. Temporal solitons in optical microresonators. *Nature Photonics*, 8 (2), **2014**, 145–152. DOI: 10.1109/CLEOE-IQEC.2013.6801769. arXiv: 1211.0733 (cited on pages 6, 7, 13–15).
- [24] F. Leo, S. Coen, P. Kockaert, S.-P. Gorza, P. Emplit, and M. Haelterman. Temporal cavity solitons in one-dimensional Kerr media as bits in an all-optical buffer. *Nature Photonics*, 4 (7), **2010**, 471–476. DOI: 10.1038/nphoton.2010.120 (cited on page 6).
- [25] T. Herr, K. Hartinger, J. Riemensberger, C. Y. Wang, E. Gavartin, R. Holzwarth, M. L. Gorodetsky, and T. J. Kippenberg. Universal formation dynamics and noise of Kerr-frequency combs in microresonators. *Nature Photonics*, 6 (7), **2012**, 480–487. DOI: 10.1038/nphoton.2012.127 (cited on page 6).
- [26] Y. K. Chembo and C. R. Menyuk. Spatiotemporal Lugiato-Lefever formalism for Kerr-comb generation in whispering-gallery-mode resonators. *Physical Review A*, 87, **2013**, 053852. DOI: 10.1103/PhysRevA.87.053852 (cited on page 6).
- [27] S. Coen, H. G. Randle, T. Sylvestre, and M. Erkintalo. Modeling of octave-spanning Kerr frequency combs using a generalized mean-field Lugiato-Lefever model. *Optics letters*, 38 (1), **2013**, 37–39. URL: <http://www.ncbi.nlm.nih.gov/pubmed/23282830> (cited on pages 6–8).
- [28] M. Haelterman, S. Trillo, and S. Wabnitz. Dissipative modulation instability in a nonlinear dispersive ring cavity. *Optics Communications*, 91 (5-6), **1992**, 401–407. DOI: 10.1016/0030-4018(92)90367-Z (cited on page 6).
- [29] T. Hansson, M. Bernard, and S. Wabnitz. Modulational Instability of Nonlinear Polarization Mode Coupling in Microresonators. 35 (4), **2018**. URL: <https://arxiv.org/pdf/1802.04535.pdf>. arXiv: arXiv:1802.04535v1 (cited on page 7).

- [30] Y. K. Chembo, I. S. Grudinin, and N Yu. Spatiotemporal dynamics of Kerr-Raman optical frequency combs. *Physical Review A*, 92 (4), **2015**, 4. DOI: 10.1103/PhysRevA.92.043818 (cited on page 7).
- [31] C. Godey, I. V. Balakireva, A. Coillet, and Y. K. Chembo. Stability analysis of the spatiotemporal Lugiato-Lefever model for Kerr optical frequency combs in the anomalous and normal dispersion regimes. *Physical Review A*, 89 (6), **2014**, 063814. DOI: 10.1103/PhysRevA.89.063814 (cited on pages 8, 10).
- [32] I. V. Barashenkov and Y. S. Smirnov. Existence and stability chart for the ac-driven, damped nonlinear Schrödinger solitons. *Physical Review E - Statistical Physics, Plasmas, Fluids, and Related Interdisciplinary Topics*, 54 (5), **1996**, 5707–5725. DOI: 10.1103/PhysRevE.54.5707 (cited on pages 8, 13).
- [33] A Coillet and Y. K. Chembo. Routes to spatiotemporal chaos in Kerr optical frequency combs. *Chaos*, 24 (1), **2014**, 5. DOI: 10.1063/1.4863298. arXiv: arXiv:1401.0927v1 (cited on page 10).
- [34] L. A. Lugiato and R Lefever. Spatial Dissipative Structures in Passive Optical Systems. *Physical Review Letters*, 58 (21), **1987**, 2209–2211 (cited on page 10).
- [35] L. Lugiato and R Lefever. Diffraction stationary patterns in passive optical systems. *Interaction of Radiation with Matter*, **1987** (cited on page 10).
- [36] W. H. Renninger and P. T. Rakich. Closed-form solutions and scaling laws for Kerr frequency combs. *Scientific Reports*, 6 (1), **2016**, 24742. DOI: 10.1038/srep24742. arXiv: 1412.4164 (cited on page 10).
- [37] S. Coen and M. Erkintalo. Universal scaling laws of Kerr frequency combs. *Optics letters*, 38 (11), **2013**, 1790–1792. DOI: 10.1364/OL.38.001790. arXiv: arXiv:1303.7078v1 (cited on page 13).
- [38] Y. Wang, F. Leo, J. Fatome, M. Erkintalo, S. G. Murdoch, and S. Coen. Universal mechanism for the binding of temporal cavity solitons, **2017**, 1–10. URL: <http://arxiv.org/abs/1703.10604>. arXiv: 1703.10604 (cited on page 14).
- [39] P. Parra-Rivas, D. Gomila, P. Colet, and L. Gelens. Interaction of solitons and the formation of bound states in the generalized Lugiato-Lefever equation. *European Physical Journal D*, 71 (7), **2017**. DOI: 10.1140/epjd/e2017-80127-5. arXiv: arXiv:1705.02619v1 (cited on page 14).
- [40] V. Brasch, T. Herr, M. Geiselmann, G. Lihachev, M. H. P. Pfeiffer, M. L. Gorodetsky, and T. J. Kippenberg. Photonic chip-based optical frequency comb using soliton Cherenkov radiation. *Science*, 351 (6271), **2016**, 357. DOI: 10.1364/CLEO_SI.2015.STh4N.1. arXiv: 1410.8598 (cited on page 15).
- [41] X. Yi, Q.-F. Yang, K. Y. Yang, M.-G. Suh, and K. Vahala. Soliton frequency comb at microwave rates in a high-Q silica microresonator. *Optica*, 2 (12), **2015**, 1078–1085 (cited on page 15).
- [42] V. E. Lobanov, G. V. Lihachev, N. G. Pavlov, A. V. Cherenkov, T. J. Kippenberg, and M. L. Gorodetsky. Harmonization of chaos into a soliton in Kerr frequency combs. *Optics Express*, 24 (24), **2016**, 27382. DOI: 10.1126/science.aah4243. arXiv: 1607.08222 (cited on page 15).
- [43] C. Joshi, J. K. Jang, K. Luke, X. Ji, S. A. Miller, A. Klenner, Y. Okawachi, M. Lipson, and A. L. Gaeta. Thermally controlled comb generation and soliton modelocking in microresonators. *Optics Letters*, 41 (11), **2016**, 2565–2568. DOI: 10.1364/OL.41.002565. arXiv: 1603.08017 (cited on page 15).
- [44] W. Wang, Z. Lu, W. Zhang, S. T. Chu, B. E. Little, L. Wang, X. Xie, M. Liu, Q. Yang, L. Wang, J. Zhao, G. Wang, Q. Sun, Y. Liu, Y. Wang, and W. Zhao. Robust soliton crystals in a thermally controlled microresonator. *Optics Letters*, 43 (9), **2018**, 2002–2005. DOI: 10.1364/OL.43.002002 (cited on page 15).

- [45] H. Guo, M. Karpov, E. Lucas, A. Kordts, M. H. Pfeiffer, V. Brasch, G. Lihachev, V. E. Lobanov, M. L. Gorodetsky, and T. J. Kippenberg. Universal dynamics and deterministic switching of dissipative Kerr solitons in optical microresonators. *Nature Physics*, 13 (1), **2017**, 94–102. DOI: 10.1038/nphys3893. arXiv: 1601.05036 (cited on page 15).
- [46] J. K. Jang, M. Erkintalo, S. G. Murdoch, and S. Coen. Writing and erasing of temporal cavity solitons by direct phase modulation of the cavity driving field. *Optics Letters*, 40 (20), **2015**, 4755–4758. DOI: 10.1364/OL.40.004755. arXiv: 1501.05289 (cited on page 15).
- [47] J. K. Jang, M. Erkintalo, S. Coen, and S. G. Murdoch. Temporal tweezing of light through the trapping and manipulation of temporal cavity solitons. *Nature Communications*, 6, **2015**, 7370. DOI: 10.1038/ncomms8370. arXiv: 1410.4836 (cited on page 15).
- [48] Y. Wang, B. Garbin, F. Leo, S. Coen, M. Erkintalo, and S. G. Murdoch. Writing and Erasure of Temporal Cavity Solitons via Intensity Modulation of the Cavity Driving Field. *arXiv*, **2018**, 1802.07428. arXiv: 1802.07428 (cited on page 15).
- [49] S. B. Papp, K. Beha, P. Del’Haye, F. Quinlan, H. Lee, K. J. Vahala, and S. A. Diddams. Microresonator frequency comb optical clock. *Optica*, 1 (1), **2014**, 10–14. DOI: 10.1364/OPTICA.1.000010. arXiv: 1309.3525 (cited on page 15).
- [50] M. G. Suh, Q. F. Yang, K. Y. Yang, X. Yi, and K. J. Vahala. Microresonator soliton dual-comb spectroscopy. *Science*, 354 (6312), **2016**, 1–5. DOI: 10.1126/science.aah6516. arXiv: 1607.08222 (cited on page 15).
- [51] P. Marin-Palomo, J. N. Kemal, M. Karpov, A. Kordts, J. Pfeifle, M. H. Pfeiffer, P. Trocha, S. Wolf, V. Brasch, M. H. Anderson, R. Rosenberger, K. Vijayan, W. Freude, T. J. Kippenberg, and C. Koos. Microresonator-based solitons for massively parallel coherent optical communications. *Nature*, 546 (7657), **2017**, 274–279. DOI: 10.1038/nature22387. arXiv: 1610.01484 (cited on page 15).
- [52] D. T. Spencer, T. Drake, T. C. Briles, J. Stone, L. C. Sinclair, C. Fredrick, Q. Li, D. Westly, B. R. Illic, A. Bluestone, N. Volet, T. Komljenovic, L. Chang, S. H. Lee, D. Y. Oh, T. J. Kippenberg, E. Norberg, L. Theogarajan, M.-g. Suh, K. Y. Yang, H. P. Martin, K. Vahala, N. R. Newbury, K. Srinivasan, J. E. Bowers, S. A. Diddams, and S. B. Papp. An optical-frequency synthesizer using integrated photonics. *Nature*, 557, **2018**, 81–85. DOI: 10.1038/s41586-018-0065-7 (cited on page 15).
- [53] J. D. Jost, T. Herr, C. Lecaplain, V. Brasch, M. H. P. Pfeiffer, and T. J. Kippenberg. Counting the cycles of light using a self-referenced optical microresonator. *Optica*, 2 (8), **2015**, 706–711. DOI: 10.1364/OPTICA.2.000706. arXiv: 1411.1354 (cited on page 15).
- [54] P. Del’Haye, A. Coillet, T. Fortier, K. Beha, D. C. Cole, K. Y. Yang, H. Lee, K. J. Vahala, S. B. Papp, and S. A. Diddams. Phase-coherent microwave-to-optical link with a self-referenced microcomb. *Nature Photonics*, 10 (June), **2016**, 1–5. DOI: 10.1038/nphoton.2016.105 (cited on page 15).
- [55] V. Brasch, E. Lucas, J. D. Jost, M. Geiselmann, and T. J. Kippenberg. Self-referenced photonic chip soliton Kerr frequency comb. *Light: Science & Applications*, 6 (1), **2017**, e16202. DOI: 10.1038/lsa.2016.202. arXiv: 1605.02801 (cited on page 15).
- [56] T. C. Briles, J. R. Stone, T. E. Drake, D. T. Spencer, C. Frederick, Q. Li, D. A. Westly, B. R. Illic, K. Srinivasan, S. A. Diddams, and S. B. Papp. Kerr-microresonator solitons for accurate carrier-envelope-frequency stabilization. *arXiv*, **2017**, 1711.06251. URL: <http://arxiv.org/abs/1711.06251>. arXiv: 1711.06251 (cited on page 15).
- [57] J. Hult. A Fourth-Order Runge-Kutta in the Interaction Picture Method for Simulating Supercontinuum Generation in Optical Fibers. *Journal of Lightwave Technology*, 25 (12), **2007**, 3770–3775. DOI: 10.1109/JLT.2007.909373 (cited on pages 17, 18, 20).
- [58] A. M. Heidt. Efficient Adaptive Step Size Method for the Simulation of Supercontinuum Generation in Optical Fibers. *Journal of Lightwave Technology*, 27 (18), **2009**, 3984–3991 (cited on pages 17, 18).

- [59] M. Hirano, T. Nakanishi, T. Okuno, and M. Onishi. Silica-Based Highly Nonlinear Fibers and Their Application. *Sel. Top. Quantum Electron.*, 15 (1), **2009**, 103–113. DOI: 10.1109/JSTQE.2008.2010241 (cited on page 20).
- [60] K. J. Blow and D Wood. Theoretical description of transient stimulated Raman scattering in optical fibers. *Quantum Electronics, IEEE Journal of*, 25 (12), **1989**, 2665–2673. DOI: 10.1109/3.40655 (cited on page 20).